Extreme Non-Wetting of Condensation-Induced Droplets on Smooth Monolayer Suspended Graphene

Haidong Wang
Tsinghua University
Daniel Orejon
University of Edinburgh
Dongxing Song
Tsinghua University
Xing Zhang
Tsinghua University https://orcid.org/0000-0002-7545-0773
Glen McHale
Northumbria University https://orcid.org/0000-0002-8519-7986
Hiroshi Takamatsu
Kyushu University
Yasuyuki Takata
Kyushu University
Khellil sefiane (ksefiane@ed.ac.uk)
University of Edinburgh

Article

Keywords: Extreme non-wetting, suspended graphene, charge transfer, suspended monolayers, wettability manipulation, double-well potential, adsorbed layers

Posted Date: April 18th, 2022

DOI: https://doi.org/10.21203/rs.3.rs-1543359/v1

Version of Record: A version of this preprint was published at Communications Materials on October 17th, 2022. See the published version at https://doi.org/10.1038/s43246-022-00294-8.

Abstract

Superhydrophobicity has only ever been achieved by a combination of chemical hydrophobicity and surface topography due to our inability to attain complete non-wetting on the smooth surface of any known material. Here, we report extreme non-wetting of condensation-induced droplets with contact angles approaching 180° on a smooth surface using suspended monolayers of graphene experimentally. Such extreme non-wetting droplets are reported exclusively on suspended monolayer graphene open to the water vapour saturated environment on both sides. Simultaneous observations of droplets condensing on monolayer and multilayer supported and suspended graphene demonstrates that this extreme non-wetting behaviour is unique to suspended monolayer graphene. These results anticipate that interactions between liquid molecules across a suspended monolayer isolated from a bulk substrate may induce extreme non-wetting beyond that possible on smooth hydrophobic or atomically flat supported monolayer surfaces.

1. Introduction

The wetting properties of solids control a wide range of processes from the self-cleaning of biological surfaces to the anti-icing and anti-fouling properties of surfaces, hence designing surfaces with desirable wettability and functionalized properties is paramount to many current industrial and everyday applications as well as developing technologies[1–3]. Chemistry is the fundamental design tool used to tailor the wettability of a surface from hydrophilic to hydrophobic with polymer materials, such as Teflon™ (polytetrafluoroethylene). The intrinsic water repellency of Teflon™ is amongst the highest known to science and is exemplified by a contact angle, θ, of ca. 120° observed when a small droplet of water partially beads up when deposited onto a flat smooth Teflon™ surface (Fig. 1a)[4]. This has been an absolute and fundamental limit (and barrier) in water repellence for any smooth material to date. To address the desire to create complete non-wetting surfaces, the last few decades of research has focused on amplifying the intrinsic hydrophobicity of surfaces through topographic structuring to create superhydrophobicity *via* a bed-of-nails ("Lotus") effect[5–9], or generating a vapor layer between the substrate and the liquid ("Leidenfrost")[10, 11].

The prevailing strategy to achieve super water repellency has been to replace the solid-liquid interface by increasing fractions of liquid-vapor interface. The presence of micro- and/or nano-structures has been an imperative requirement to confer a surface with superhydrophobic properties starting with contact angles for water and other fluids on smooth surfaces limited to 120° or less[12–15]. The principle of these surfaces is to manipulate surface structure and/or the intrinsic wettability of the outermost surface so that capillary penetration between surface features is unfavorable[8,14–16]. The droplet then bridges across tips of surface features and effectively sits on a composite of the solid and air (Fig. 1b). In the simplest model for a droplet resting above the surface features in the Cassie-Baxter state, the cosine of the observed macroscopic contact angle, θ_{CB}, is a weighted average using the solid surface fraction, ϕ_s, and the air fraction, $(1 - \phi_s)$[16, 17]. Thus, the contact angle approaches complete non-wetting when the

solid surface fraction vanishes. Conceptually, when the length scale of surface features becomes vanishingly small a droplet supported entirely by air and a droplet surrounded by only air will adopt a completely spherical shape with $\theta_{CB} \rightarrow 180^{o}$, under the action of surface tension to minimize its surface free energy. Such an ideal situation is similarly observed when a droplet touches an extremely hot surface, which is above its Leidenfrost point[7, 8] or at ambient temperature on a low pressure environment[18, 19] and an instantaneous vaporization of a layer of water occurs resulting in a beaded up spherical droplet resting on a layer of its own vapor (Fig. 1c).

Whilst the current strategy to achieve complete non-wetting is able to produce completely beaded up droplets, it does not address the fundamental question of how to achieve superhydrophobicity or extreme non-wetting on a continuous and smooth solid surface. It does, however, highlight that a key issue is the interaction of the droplet with the solid substrate. In that regard, we anticipate that reducing the thickness of the substrate, *t*, to a size comparable or less than the interaction length scale between the liquid and solid may effectively remove the interaction with the substrate or surroundings with the consequent expected change from wetting to extreme non-wetting behaviour. However, for a membrane-like substrate its rigidity scales as t^3, and so it completely wraps itself around the liquid droplet even if the substrate is hydrophobic, such as Teflon™ (Fig. 1d); this effect is known as *Capillary Origami*[20–22]. In view of the above, a strategy for exploring wetting and water repellency, beyond that possible on smooth hydrophobic substrates and without using topographic structuring, is to i) use a membrane of a material allowing for long range interactions beyond its thickness, and ii) suspend the membrane across a gap between two surfaces to avoid the occurrence of Capillary Origami.

To demonstrate this strategy, we therefore created mono and multilayers of graphene on a silicon substrate patterned with holes and trenches. The suspended monolayer graphene may have negligible interaction with water on top, known as the “wetting transparency” suggested in the literature[23–25]. We were able to create solid membranes of differing thicknesses (i.e. layers) either backed by silicon or bridging across gaps and so backed by vapor (or vacuum). By condensing droplets across the entirety of the surface it was then possible to investigate both the effects of membrane thickness and the solid (i.e. supported) *versus* vapor (or vacuum) backing of the membrane (i.e. suspended) on the observed wetting properties (Fig. 1e,f).

2. Results And Discussion

For our experimental observations we used monolayer (1L), 2 layers (2L) and 4 layers (4L) of graphene and multilayer graphite (ML) supported and suspended over holes and trenches. For simplicity, we henceforth refer to suspended graphene with the superscript ^{sus} and to supported graphene with the subscript $_{sup}$. Surface characterization of the fabricated 1L substrate is shown in Fig. 2. More details and description of the surface fabrication and characterization on the rest of the fabricated substrates are given in Section 4.1 Substrate Fabrication and 4.2. Sample Characterization of 1L Suspended Graphene

within Section 4 Experimental Section/Methods and within the accompanying Supplementary Information SI-1 and SI-2, respectively.

Direct contact angle measurements of sessile droplets on suspended graphene ($1L^{sus}$) have not been reported to date as a consequence of the impossibility to create large suspended regions, by our current fabrication and cleaning procedures, large enough to allow for macroscopic sessile droplet deposition or microgoniometry direct wettability measurements. Note that the minimum size of droplets generated via microgoniometry is at least one order of magnitude greater than the fabricated area of $1L^{sus}$ [26]. Thus, to date, the wettability of graphene has been assessed exclusively by indirect methods such as measuring the contact angle of a bubble immersed in water in contact with monolayer graphene[27] or rolling a droplet of water over monolayer graphene powder[28]. Hereafter, to allow for the immediate and intimate visualization of the interactions between droplets with sizes in the order of micrometers in diameter or smaller (femtoliter droplets) and the different suspended and supported graphene substrates, we make use of the excellent spatial resolution provided by Environmental Scanning Electron Microscopy (ESEM) (FEI Versa 3D™, Hillsboro, Oregon, U.S.A.). Note that Zhang et al. recently reported on the wettability of suspended monolayer graphene over a holey substrate atop a TEM grid, i.e., closed holes, making use of ESEM at the same time of this submission[29]. ESEM experimental observations on suspended monolayer graphene over a holey substrate atop a TEM grid with closed holes similar to those reported by Zhang et al. were also carried out in our work and can be seen in **Figure S8** in the accompanying Supporting Information SI-5. To highlight is the remarkable agreement on the contact angles reported by Zhang et al. [29] and those reported in **Figure S8** for droplets sitting fully on the suspended graphene droplets resting partially on both suspended and supported graphene with closed holes (See Fig. 4 providing a direct comparison between the contact angle measurements for monolayer graphene suspended over closed holes of this work and that of Zhang et al. [29]).

Figure 3 | **ESEM experimental observations of condensation** on **(a-c)** $1L^{sus}$, (d) $2L^{sus}$, **(e)** $4L^{sus}$, and **(f)** ML^{sus} in time (see Supplementary Videos 1 to 6). Non-wetting water droplets are only observed on suspended graphene ($1L^{sus}$). We note here that experimental observations on **(a-b)** and **(c)** correspond to 2 different samples prepared by the same fabrication procedure reported in section 4.1 Sample Fabrication and in the accompanying Supplementary Information SI-1. Relative condensation time with respect to the first frame, environmental pressure and scale bars reported from ESEM experimental observations are included for each frame (more details on the ESEM experimental procedure and observations can be found in Section 4.3 ESEM Experimental Observations and within the Supplementary Information SI-3).

Figure 3a,b,c- show droplets growing in the non-wetting regime following the constant contact angle mode (CCA) on $1L^{sus}$, whereas on $2L^{sus}$, $4L^{sus}$, and ML^{sus} (Fig. 3d,e,f) droplets grow also in the CCA mode

but in the partial wetting regime. The Supplementary Videos 1 to 6 contain the ESEM images of the 6 panels (a-f) presented in Fig. 3. Videos were captured at approximately 1 frame every 5 seconds highlighting the quasi-static state of our observations. Here, we define “non-wetting droplet” as a droplet with a measured contact angle (or advancing contact angle henceforth referred to as contact angle) larger than 120º, which was known to be the hydrophobic limit/barrier for any smooth hydrophobic surface set by Teflon™ [4, 11]. Non-wetting droplets were found to be reproducible on the same sample even after five condensation-evaporation cycles. This is a remarkable evidence of the difference in wettability between $1L^{sus}$ when compared to $1L_{sup}$. This is further ascertained with the observations of the main droplet in Fig. 3b, which initially grows in the non-wetting regime while the base of the droplet is on $1L^{sus}$, and as the droplet grows bigger and the triple contact line touches the supported region ($1L_{sup}$) the droplet suddenly spreads, *i.e.*, it transitions from non-wetting on $1L^{sus}$ to partial wetting on $1L_{sup}$. The largest contact angle of a droplet on $1L^{sus}$ approaches 180º as in the right side of Fig. 3b, which resembles the ideal shape of a free-standing droplet in vacuum and/or in air. To further confirm that the presence of extreme non-wetting droplets is solely an inherent quality of $1L^{sus}$, Fig. 4 includes independent contact angle measurements on both 1L, 2L, 4L and ML suspended and supported graphene at different condensation intervals. In addition, Fig. 4 shows experimental observations of droplets on 1L, 2L, 4L and ML samples simultaneously on both supported and suspended regions. The suspended and supported graphene areas are marked in Fig. 4 and they can be clearly distinguished by the position of the edges.

Figure 4 shows that droplets on $1L^{sus}$ have contact angles as high as 175º while droplets on $1L_{sup}$ display contact angles close to or below 90º. In the case of 2L, 4L and ML, contact angles of droplets on both suspended and supported samples are practically the same and in the partial wetting regime with values close to 90º or below 90º, which are also similar to those reported here for water droplets on $1L_{sup}$ and consistent with the literature[22]. Non-wetting contact angles on $1L^{sus}$ reported in this work and in Fig. 4 differ from wetting contact angles reported on partially suspended monolayer graphene (solid surface fractions as low as 5%) in the work of Ondarçuhu *et al.*[30]. This is mainly due to the complete suppression of any substrate interaction, which is entirely removed from underneath the footprint of the droplets coupled with the presence of an adsorbed layer of water above and below the $1L^{sus}$ as per the high humidity environmental conditions studied under ESEM. Note that spreading of a non-wetting droplet growing on $1L^{sus}$ was observed once the advancing contact line of the non-wetting droplet reached the $1L_{sup}$ as shown in Fig. 3b. In addition, the agreement between this work and that of Zhang et al.[29] on the wettability of suspended monolayer graphene over closed holes is further provided within Fig. 4. In addition, the occurrence of partially wetting droplets reported on $1L^{sus}$ with open holes is attributed to the current inability of the scientific community of fabricating 100% full crystalline, wrinkle free and clean suspended graphene of the sizes required. The presence of amorphous regions, wrinkles and hydrocarbons may induce surface defects which in turn decrease the energy barrier for nucleation

favoring condensation on those regions[31, 32]. This provides a plausible and reasonable explanation for the occurrence of the bimodal contact angle distribution showing both wetting and non-wetting droplets on the same $1L^{sus}$.

In macroscopic wetting studies, to assess the extent of pinning the droplet contact line is advanced or receded by addition or withdraw of liquid to the droplet. In contrast, in the ESEM approach the contact line advances by condensation of molecules and, significantly, can overcome small irregularities on the surface. Although nanoscale defects can induce pinning[33], the quasi-steady droplet growth imposed where condensing molecules build up at the triple phase contact line and at the liquid-gas interface can overcome the pinning energy barrier via thermal fluctuations and/or external forces[34]. Additionally, it is worth noting that condensation shall preferentially take place on such topological or chemical defects; however, based on the Kelvin equation, the cluster size necessary for nucleation is orders of magnitude larger than any of the defects measured on our $1L^{sus}$ reported in Fig. 2b. To estimate the extent of this we consider the critical droplet radius for nucleation, r_e, by making use of the Kelvin equation

$$r_e = {2T_v\gamma_{lv}}\Big/{h_{fg}\rho_l\Delta T}$$

where T_v is the temperature of the vapor, γ_{lv} is the liquid-vapor interfacial tension, h_{fg} the latent heat of vapor to liquid phase-change, ρ_l the density of the liquid and ΔT the subcooling temperature[32, 35]. In the present conditions where the ESEM works near the liquid-vapor saturation curve[36], r_e is of the order of tens of nanometers, which is two orders of magnitude greater than the average of the defects found in $1L^{sus}$ (see calculations on r_e versus ΔT in **Figure S10** in the accompanying Supporting Information SI-5, and AFM characterization of $1L^{sus}$ in Fig. 2b and in the accompanying Supporting Information SI-2.2). This estimation points out that the cluster size of the molecules required for nucleation is orders of magnitude greater than the defects present. This suggests that pinning of the contact line by small defects on the nm scale is unlikely to explain the observation of non-wetting droplets on $1L^{sus}$.

Moreover, the simultaneous occurrence of spherical non-wetting and partial wetting droplets on $1L^{sus}$ and $1L_{sup}$, respectively, shown in Fig. 4 within the same frame under the same temperature and pressure conditions provides evidence for unique non-wetting properties of $1L^{sus}$. Further, nanoscale defects increase in size and number as the number of graphene layers increase; hence if pinning on such defects were to be the reasons for the non-wetting droplets observed, such behaviour should have been reported on the rest of supported and suspended graphene substrates with multiple layers. Despite the greater degree of nanoscopic defects and roughness of $1L_{sup}$, 2L, 4L and ML, when compared to $1L^{sus}$ (see Fig. 2 and **Figure S5** and **S6**), which should promote contact line pinning, the lack of non-wetting droplets on of $1L_{sup}$, 2L, 4L and ML (0 drops out of more than 2000 observations) suggests that surface contamination, roughness and/or pinning may not be the mechanism for the extreme non-wetting behaviour reported here on $1L^{sus}$. An intrinsic limitation in these experiments is that because of the small volume of the

imaged droplets limited by the $1L^{sus}$ sample size and the quasi-steady ESEM imaging technique utilized, any receding of the triple contact line before complete evaporation cannot be captured.

Theoretical trends based on the Lennard-Jones (L-J) potential from Ref. 9 and 22 offer a reasonable explanation for the contact angles of wetting droplets reported on multilayer graphene but cannot explain the case of suspended monolayer[10, 24]. Under ESEM operating conditions, the environment is saturated with water vapor and hence the suspended graphene layer is surrounded by water vapor where the polar interactions of water molecules above and below graphene could act across this one atomic layer, as suggested in recent works[23]. Recent ESEM experiment of water condensation on single side of graphene[29] and additional experiments reproducing the conditions reported in Ref. 29 carried out in this investigation so to validate our approach (**Figure S8** in the Supplementary Information) indicate that non-wetting droplets can be seen exclusively on suspended monolayers open to the ambient on both sides and not on monolayer graphene where either of the sides is closed to the environment. The present findings may be relevant to further understanding monolayer wettability and offer additional elements on the wetting translucency and the high slippage of graphene upon interaction with water molecules as reported recently[23,37–39].

3. Conclusions

Direct experimental observations of micrometer/picoliter droplets condensing on monolayer suspended graphene are used to characterize its inherent wettability. Extreme non-wetting droplets with contact angles as high as 175° are reported exclusively on a smooth atomically flat one-layer suspended graphene, whereas wetting droplets with contact angles below 90° are reported on supported monolayer and on supported and suspended multiple layers graphene. Experimental observations demonstrate that non-wetting of water droplets on smooth monolayer may be possible by removing the water-surface interactions beyond the first surface layer in the case of graphene. This suggests the maximum contact angle attainable on a smooth hydrophobic surface may not be limited to that of Teflon™.

The present observations open the door to wettability manipulation through suspended graphene. This could be achieved through control of the environment behind the suspended graphene layer such as the use of microfluidics and calls for the further investigations on other monolayer materials.

Experimental Section/Methods

Substrate fabrication

The fabrication procedure was as follows: monolayer graphene was grown on copper foil by using standard chemical vapor deposition (CVD) method[40]. Then, the graphene was transferred onto a SiO_2/Si target substrate by using common poly(methyl-methacrylate) (PMMA) transfer method. To create well defined holes and trenches, prior to the graphene transfer procedure, the SiO_2/Si target substrate was subjected to electron beam (EB) lithography and reactive ion etching (RIE). After the transfer procedure

and in order remove the PMMA layer, the SiO_2/Si target sample coated with graphene and PMMA was dipped into acetone at ~ 50°C for more than 4 hours. The warmth of the solvent as well as the sufficient immersion time induced the thorough PMMA removal and minimizes contamination and residual PMMA left on the graphene[40, 41]. To avoid the rupture of the membrane, the final step consisted on drying the graphene sample by using an HITACHI HCP-2 supercritical point dryer. The high quality of the suspended graphene sample was confirmed by Scanning Electron Microscopy (SEM), Atomic Force Microscopy (AFM), Tunneling Electron Microscopy (TEM) and Raman spectroscopy (see Fig. 2 in the main text). In addition to monolayer graphene (1L), double-layer graphene (2L) and four-layer (4L) samples were prepared by stacking the monolayer graphene several times following the same CVD growth and the same PMMA transfer procedures reported above[41]. On the other hand, multi-layer graphite (ML) sample was prepared by mechanical exfoliation method and then transferred onto the substrate.

Sample Characterization of 1L Suspended Graphene

Within the Supplementary Information, we follow the same nomenclature as established within the main text. We do henceforth refer to suspended graphene with the superscript ^{sus} and to supported graphene with subscript $_{sup}$. From the surface characterization by optical microscopy and SEM shown in Fig. 2a (main text), the successful fabrication of both $1L^{sus}$ and $1L_{sup}$ is demonstrated. 1L graphene was completely suspended ($1L^{sus}$) over holes with up to 5 μm in diameter and over trenches of 5 μm in width and tens of micrometers in length. From Fig. 2a (main text), we note the optical transparency of graphene to SEM as previously reported[42]. When looking into AFM topography characterization, Fig. 2b (main text) shows that the roughness of $1L^{sus}$ is slightly smaller than that of $1L_{sup}$ on the smooth substrate. The latter indicates that the suspended graphene membrane is quite smooth and most of the polymer residues have been removed from the surface. In addition, the lower-right inset of Fig. 2c (main text) presents a high-resolution TEM image of $1L^{sus}$ showing the clean lattice with perfect honeycomb structure, which is characteristic of high quality graphene. From Fig. 2c (main text), some nanoscale islands of residues can be perceived on the graphene, which may serve as nuclei for the condensation experiment. In addition, ED pattern (top-right inset in Fig. 2c (main text)) exhibits the perfect 6-fold symmetry of the carbon atoms, which is also characteristic of high quality graphene. Finally, Fig. 2d (main text) shows Raman spectra of 1L, 2L, 4L and ML. For 1L, the height of the 2D peak (~ 2700 cm^{-1}) is almost twice as large as that of the G peak (~ 1580 cm^{-1}) evidencing the monolayer structure[42]. The height ratio between 2D and G peaks decreases as the number of graphene layers increase. For ML sample, the 2D peak is much wider and shorter than the G peak, which is consistent with literature. It is worth noting that the D peak (~ 1300 cm^{-1}) is almost absent for all four samples, which highlights the negligible defects of the carbon lattice. Next, we include additional optical microscopy, SEM and AFM topography characterization of 1L, 2L, 4L and ML graphene fabricated substrates. More details on the Sample Characterisation can be found in SI-2. Sample Characterisation of 1L Suspended Graphene in the Accompanying Supporting Information.

ESEM Experimental Observations

Experimental observations of condensation were undertaken in an Environmental Scanning Electron Microscope FEI Versa 3D™ (Hillsboro, Oregon, U.S.A.), where temperature of the surface and the vapor pressure of the environment could be finely controlled. Graphene sample was fixed to a 45° sample holder using double side carbon tape and then the sample holder was fixed onto the Peltier stage, to allow for experimental observations at a tilting angle of ca. 80° with respect to the electron beam. The temperature of the Peltier stage and the water vapor pressure were precisely controlled with the xT Microscope Control software with an average deviation from the equilibrium liquid-vapor curve of ± 0.3 ºC and ± 16 Pa and a maximum deviation of ± 0.7 ºC and ± 30 Pa [36]. The initial temperature of the Peltier stage was set to 0 ºC on the graphene surface, which was further confirmed by additional measurements with an external thermocouple. Once the graphene sample was placed on the Peltier stage, the chamber was vacuumed for several minutes to ~ 10^{-3} Pa, removing any presence of non-condensable gases, and thereafter the chamber was set into Environmental Scanning Electron Microscopy (ESEM) mode. Then, the vapor pressure was slowly increased from ~ 100 Pa to ~ 600 Pa until the condensation occurred. The pressure rate was increased at the lowest rate of 6 Pa/min. The dynamics of droplet growth was recorded by the software at 1 frame every ca. 3 seconds. After each experimental observation, in order to evaporate the water condensed, the vapor pressure was decreased at low rates to avoid the rupture of graphene. More details on the Sample Characterisation via ESEM experimental observations can be found in SI-3. ESEM Experimental Observations in the Accompanying Supporting Information.

Experimental Section/methods

Substrate fabrication

The fabrication procedure was as follows: monolayer graphene was grown on copper foil by using standard chemical vapor deposition (CVD) method[40]. Then, the graphene was transferred onto a SiO_2/Si target substrate by using common poly(methyl-methacrylate) (PMMA) transfer method. To create well defined holes and trenches, prior to the graphene transfer procedure, the SiO_2/Si target substrate was subjected to electron beam (EB) lithography and reactive ion etching (RIE). After the transfer procedure and in order remove the PMMA layer, the SiO_2/Si target sample coated with graphene and PMMA was dipped into acetone at ~50 °C for more than 4 hours. The warmth of the solvent as well as the sufficient immersion time induced the thorough PMMA removal and minimizes contamination and residual PMMA left on the graphene[40,41]. To avoid the rupture of the membrane, the final step consisted on drying the graphene sample by using an HITACHI HCP-2 supercritical point dryer. The high quality of the suspended graphene sample was confirmed by Scanning Electron Microscopy (SEM), Atomic Force Microscopy (AFM), Tunneling Electron Microscopy (TEM) and Raman spectroscopy (see Fig. 2 in the main text). In addition to monolayer graphene (1L), double-layer graphene (2L) and four-layer (4L) samples were prepared by stacking the monolayer graphene several times following the same CVD growth and the same PMMA transfer procedures reported above[41]. On the other hand, multi-layer graphite (ML) sample was prepared by mechanical exfoliation method and then transferred onto the substrate.

Sample Characterization of 1L Suspended Graphene

Within the Supplementary Information, we follow the same nomenclature as established within the main text. We do henceforth refer to suspended graphene with the superscript ^{sus} and to supported graphene with subscript $_{sup}$. From the surface characterization by optical microscopy and SEM shown in Fig. 2a (main text), the successful fabrication of both $1L^{sus}$ and $1L_{sup}$ is demonstrated. 1L graphene was completely suspended ($1L^{sus}$) over holes with up to 5 μm in diameter and over trenches of 5 μm in width and tens of micrometers in length. From Fig. 2a (main text), we note the optical transparency of graphene to SEM as previously reported[42]. When looking into AFM topography characterization, Fig. 2b (main text) shows that the roughness of $1L^{sus}$ is slightly smaller than that of $1L_{sup}$ on the smooth substrate. The latter indicates that the suspended graphene membrane is quite smooth and most of the polymer residues have been removed from the surface. In addition, the lower-right inset of Fig. 2c (main text) presents a high-resolution TEM image of $1L^{sus}$ showing the clean lattice with perfect honeycomb structure, which is characteristic of high quality graphene. From Fig. 2c (main text), some nanoscale islands of residues can be perceived on the graphene, which may serve as nuclei for the condensation experiment. In addition, ED pattern (top-right inset in Fig. 2c (main text)) exhibits the perfect 6-fold symmetry of the carbon atoms, which is also characteristic of high quality graphene. Finally, Fig. 2d (main text) shows Raman spectra of 1L, 2L, 4L and ML. For 1L, the height of the 2D peak (~2700 cm^{-1}) is almost twice as large as that of the G peak (~1580 cm^{-1}) evidencing the monolayer structure[42]. The height ratio between 2D and G peaks decreases as the number of graphene layers increase. For ML sample, the 2D peak is much wider and shorter than the G peak, which is consistent with literature. It is worth noting that the D peak (~1300 cm^{-1}) is almost absent for all four samples, which highlights the negligible defects of the carbon lattice. Next, we include additional optical microscopy, SEM and AFM topography characterization of 1L, 2L, 4L and ML graphene fabricated substrates. More details on the Sample Characterisation can be found in SI-2. Sample Characterisation of 1L Suspended Graphene in the Accompanying Supporting Information.

ESEM Experimental Observations

Experimental observations of condensation were undertaken in an Environmental Scanning Electron Microscope FEI Versa 3D^{TM} (Hillsboro, Oregon, U.S.A.), where temperature of the surface and the vapor pressure of the environment could be finely controlled. Graphene sample was fixed to a 45° sample holder using double side carbon tape and then the sample holder was fixed onto the Peltier stage, to allow for experimental observations at a tilting angle of ca. 80° with respect to the electron beam. The temperature of the Peltier stage and the water vapor pressure were precisely controlled with the xT Microscope Control software with an average deviation from the equilibrium liquid-vapor curve of ± 0.3

ºC and ± 16 Pa and a maximum deviation of ± 0.7 ºC and ± 30 Pa [36]. The initial temperature of the Peltier stage was set to 0 ºC on the graphene surface, which was further confirmed by additional measurements with an external thermocouple. Once the graphene sample was placed on the Peltier stage, the chamber was vacuumed for several minutes to ~10^{-3} Pa, removing any presence of non-condensable gases, and thereafter the chamber was set into Environmental Scanning Electron Microscopy (ESEM) mode. Then, the vapor pressure was slowly increased from ~100 Pa to ~600 Pa until the condensation occurred. The pressure rate was increased at the lowest rate of 6 Pa/min. The dynamics of droplet growth was recorded by the software at 1 frame every ca. 3 seconds. After each experimental observation, in order to evaporate the water condensed, the vapor pressure was decreased at low rates to avoid the rupture of graphene. More details on the Sample Characterisation via ESEM experimental observations can be found in SI-3. ESEM Experimental Observations in the Accompanying Supporting Information.

Declarations

Acknowledgements

The work was supported by the National Youth 1000 Talents Program in China, and National Natural Science Foundation of China Grant Nos. 51976096, 51827807. K.S. and D.O. acknowledge the support received from the European Space Agency (ESA) within the project Convection and Interfacial Mass Exchange (EVAPORATION) with ESA Contract Number 4000129506/20/NL/PG. D.O. acknowledges the support received from JSPS KAKENHI Early Career Scientists with Grant No. JP18K13073. D.O. and Y.T. acknowledge the support receive from the International Institute for Carbon-Neutral Energy Research (WPI-I2CNER), sponsored by the Japanese Ministry of Education, Culture, Sports, Science and Technology MEXT.

Funding

National Youth 1000 Talents Program in China, Grant No. 51976096 (HW)

National Natural Science Foundation of China, Grant No. 51827807 (HW, XZ)

European Space Agency (ESA), Convection and Interfacial Mass Exchange (EVAPORATION), ESA Contract No. 4000129506/20/NL/PG

JSPS KAKENHI Early Career Scientists with Grant No. JP18K13073

Author Contributions

Conceptualization: KS

Methodology: KS, HW, DO.

Investigation: HW, DO, GM

Visualization: HW, DO

Funding acquisition: HW, XZ, YT, KS

Project administration: KS

Supervision: KS, YT, HT, XZ

Writing – original draft: HW, DO, KS, GM

Writing – review & editing: HW, DO, DS, XZ, GM, HT, YT, KS

Competing Interests Statement

The authors declare no conflict of interest or competing financial interests associated to this publication.

Data and materials availability

Supporting Information is available from the Wiley Online Library or from the author.

Correspondence and requests for materials should be addressed to K.S. ksefiane@ed.ac.uk

Supplementary Materials

SI-1. Substrate Fabrication

SI-2. Sample Characterization of 1L Suspended Graphene

SI-2.1 Sample Characterization by Optical Microscopy and SEM

SI-2.2 AFM Topography Characterization of Surface Roughness of Graphene

SI-3. ESEM Experimental Observations

SI-4. Statistical Analysis

SI-5. Minimum Radius for Nucleation

Movies S1 to S6

References

1. Nishimoto, S. & Bhushan, B. Bioinspired self-cleaning surfaces with superhydrophobicity, superoleophobicity, and superhydrophilicity. RSC Adv. **3**, 671–690 (2013).
2. Kirschner, C. M. & Brennan, A. Bio-inspired antifouling strategies. Annu. Rev. Mater. Res. **42**, 211–219 (2012).
3. Yao, X., Song, Y. & Jiang, L. Applications of bio-inspired special wettable surfaces, Adv. Matter. **23**, 719–734 (2011).
4. Adamson, A. W. & Gast, A. P. *Physical Chemistry of Surfaces* (Wiley-Blackwell, 1997).
5. Barthlott, W. & Neinhuis, C. Purity of the sacred lotus, or escape from contamination in biological surfaces. Planta **202**, 1–8 (1997).
6. Neinhuis, C. & Barthlott, W. Characterization and distribution of water-repellent self-cleaning plant surfaces. Ann. Bot. **79**, 667–677 (1997).
7. Onda, T., Shibuichi, S., Satoh, N. & Tsujii, K. Super-water-repellent fractal surfaces. Langmuir **12**, 2125–2127 (1996).
8. Lafuma, A. & Quéré, D. Superhydrophobic states. Nat. Mater. **2**, 457–460 (2003).
9. Wang, S. & Jiang, L. Definition of Superhydrophobic States. Adv. Mater. **19**, 3423–3424 (2007).
10. Leidenfrost, J. G. *De aquae communis nonnullis qualitatibus tractatus* (Duisburgh 1756).
11. Biance, A. -L., Clanet, C. & Quéré, D. Leidenfrost drops. Phys. Fluids **15**, 1632–1637 (2003).
12. Öner, D. & McCarthy, T. J. Ultrahydrophobic surfaces. Effects of topography length scales on wettability. Langmuir **16**, 7777–7782 (2000).
13. Tuteja, A., Choi, W., Ma, M., Mabry, J. M., Mazzella, S. A., Rutledge, G. C., McKinley, G. H. & Cohen, R. E. Designing superoleophobic surfaces. Science **318**, 1618–1622 (2007).
14. Liu, T. “Leo” & Kim, C. -J. “CJ”. Turning a surface superrepellent even to completely wetting liquids. *Science* **346**, 1096–1100 (2014).
15. Yan, X. et al. Atmosphere-mediated superhydrophobicity of rationally designed micro/nanostructured surfaces. ACS Nano **13**, 4160–4173 (2019).
16. Quéré, D. Wetting and roughness. Annu. Rev. Mater. Res. **38**, 71–99 (2008).
17. Saran, R., Fox, D., Zhai, L. & Chanda, D., Organic Non-Wettable Superhydrophobic Fullerite Films, Adv. Mater. **33**, 2102108 (2021).
18. Schutzius, T. M., Jung, S., Maitra, T., Graeber, G., Köhme, M. & Poulikakos, D. Spontaneous droplet trampolining on rigid superhydrophobic surfaces. Nature **527**, 82–85, 2015.
19. Celestini, F., Frisch, T. & Pomeau, Y. Room temperature water Leidenfrost droplets. Soft Matter **9**, 9535–9538, 2013.

20. Py, C., Reverdy, P., Doppler, L., Bico, J., Roman, B. & Baroud, C. Capillary Origami: Spontaneous wrapping of a droplet with an elastic sheet. Phys. Rev. Lett. **98**, 2–5 (2007).
21. Gao, L. & McCarthy, T. J. Teflon is hydrophilic. Comments on definitions of hydrophobic, shear versus tensile hydrophobicity and wettability characterization. Langmuir **24**, 9183–9188 (2008).
22. McHale, G. All solids, including Teflon, are hydrophilic (to some extent), but some have roughness induced hydrophobic tendencies. Langmuir **25**, 7185–7187 (2009).
23. Rafiee, J., Mi, X., Gullapalli, H., Thomas, A. V., Yavari, F., Shi, Y., Ajayan, P. M. & Koratkar, N. A. Wetting transparency of graphene. Nat. Mater. **11**, 217–222 (2012).
24. Shih, C. -J., Want, Q. -H., Lin, S., Park, K. –C., Jin, Z., Strano, M. S. & Bankschtein, D. Breakdown in the wetting transparency of graphene. Phys. Rev. Lett. **109**, 176101 (2012).
25. Shih, C. -J., Want, Q. -H., Lin, S., Park, K. –C., Jin, Z., Strano, M. S. & Bankschtein, D. Erratum: Breakdown in the wetting transparency of graphene [Phys. Rev. Lett. **109**, 176101 (2012)]. *Phys. Rev. Lett.* **115**, 49901 (2015).
26. Yan, X. et al. Droplet jumping: effects of droplet size, surface structure, pinning, and liquid properties. ACS Nano **19**, 1309–1323 (2019).
27. Prydatko, A. V., Belyaeva, L. A., Jiang, L., Lima, L. M. C. & Scheider, G. F. Contact angle measurement of free-standing square-millimeter single-layer graphene. Nature Commun. **9**, 4185 (2018).
28. Bera, B., Shahidzadeh, N., Mishra, H., Belyaeva, L. A., Schneider, G. F. & Bonn, D. Wetting of water on graphene nanopowders of different thicknesses. Appl. Phys. Lett. **112**, 151606 (2018).
29. Zhang et al. Intrinsic Wettability in Pristine Graphene. Adv. Mater. 2103620 (2021).
30. Ondarçuhu, T., Thomas, V., Nuñez, M., Dujardin, E., Rahman, A., Black, C. T. & Checco, A. Wettability of partially suspended graphene. Sci Rep 6, 24237 (2016).
31. Li, Z., et al. Effect of airborne contaminants on the wettability of supported graphene and graphite. Nature Materials **12**, 925–931 (2013).
32. Fisher, L. R. & Israelachvili, J.N. Direct experimental verification of the Kelvin equation for capillary condensation Nature **277**, 548–549 (1979).
33. Wang, Y. J., Guo, S., Chen, H.- Y. & Tong, P. Understanding contact angle hysteresis on an ambient solid surface, Phys. Rev. E **93**, 052802 (2016).
34. Giacomello, A., Schimmele, L. & Dietrich S. Wetting hysteresis induced by nanodefects. *Proceedings of the National Academy of Sciences* **113** (3) E262-E271 (2016).
35. Maa, J. R., Droplet Size Distribution and Heat Flux of Dropwise Condensation, The Chemical Engineering Journal **16**, 171–176 (1978).
36. Orejon, D., Shardt, O., Waghmare, P. R., Kumar Gunda, N. S., Takata, Y. & Mitra, S. K., Droplet migration during condensation on chemically patterned micropillars, RSC Adv. **6**, 36698–36704 (2016).
37. Kim, G. -T., Gim, S. -J., Cho, S. -M., Koratkar, N. & Oh, I. -K. Wetting-transparent graphene films for hydrophobic water-harvesting surfaces. Advanced Materials **26**, 5166–5172 (2014).

38. Tocci, G., Joly, L. & Michaelides, A. Friction of water on graphene and hexagonal boron nitride from *Ab Initio* methods: very different slippage despite very similar interface structures. Nano Lett. **14**, 6872–6877 (2014).
39. Secchi, E., Marbach, S., Niguès, A., Stein, D., Siria, A. & Bocquet, L. Massive radius-dependent flow slippage in carbon nanotubes. Nature **537**, 210–213 (2016).
40. Srivastava, A., Galande, C., Ci, L., Song, L., Rai, C., Jariwala, D., Felly, K. F. & Ajayan, P. M. Novel liquid precursor-based facile synthesis of large-area continuous, single, and few-layer graphene films. Chem. Mater. **22**, 3457–3461 (2010).
41. Lin, Y.-C., Jin, C., Lee, J.-C., Jen, S.-F., Suenaga, K. & Chiu, P.-W.. Clean transfer of graphene for isolation and suspension. ACS Nano **5**, 2362–2368 (2011).
42. Nair, R. R., Blake, P, Grigorenko, A. N., Novoselov, K. S., Booth, T. J., Stauber, T., Peres, N. M. R. & Geim A. K. Fine structure constant defines visual transparency of graphene. Science **320**, 1308–1308 (2008).
43. Li, Q.-Q., Zhang, X., Han, W.-P., Lu, Y., Shi, W., Wu, J.-B. & Tan, P.-H. Raman spectroscopy at the edges of multilayer graphene. Carbon **85**, 221–224 (2015).

Figures

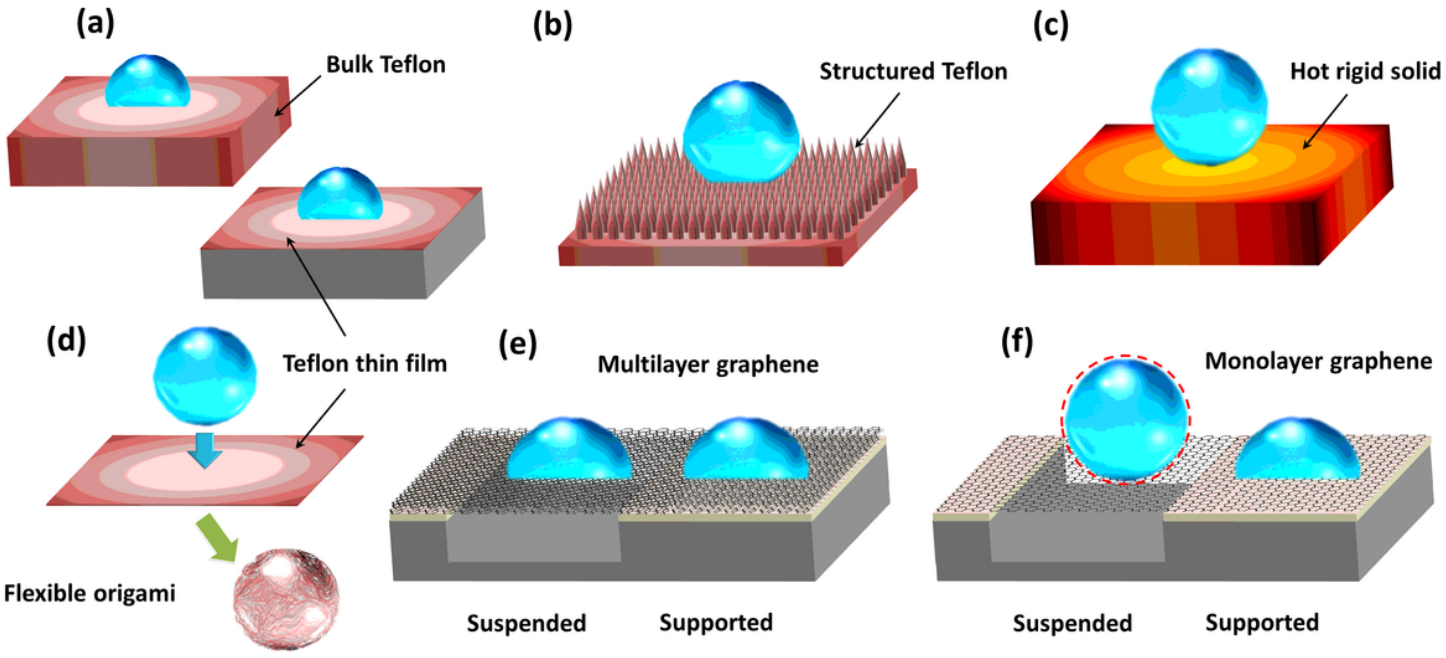

Figure 1

Schematic representation of wetting and non-wetting of liquids on various materials: (a) non-wetting on bulk rigid TeflonÔ and on surface coated with a thin film of TeflonÔ, **(b)** non-wetting on superhydrophobic structured TeflonÔ bed of nails, **(c)** non-wetting on an extremely hot rigid material, **(d)** wetting of hydrophobic TeflonÔ thin film wrapping itself around the droplet as in *Capillary Origami*[20], **(e)** wetting on

suspended and on supported multilayer graphene, and **(f)** wetting on supported monolayer graphene and non-wetting on suspended monolayer graphene where non-wetting droplet is highlighted by a red dashed circle.

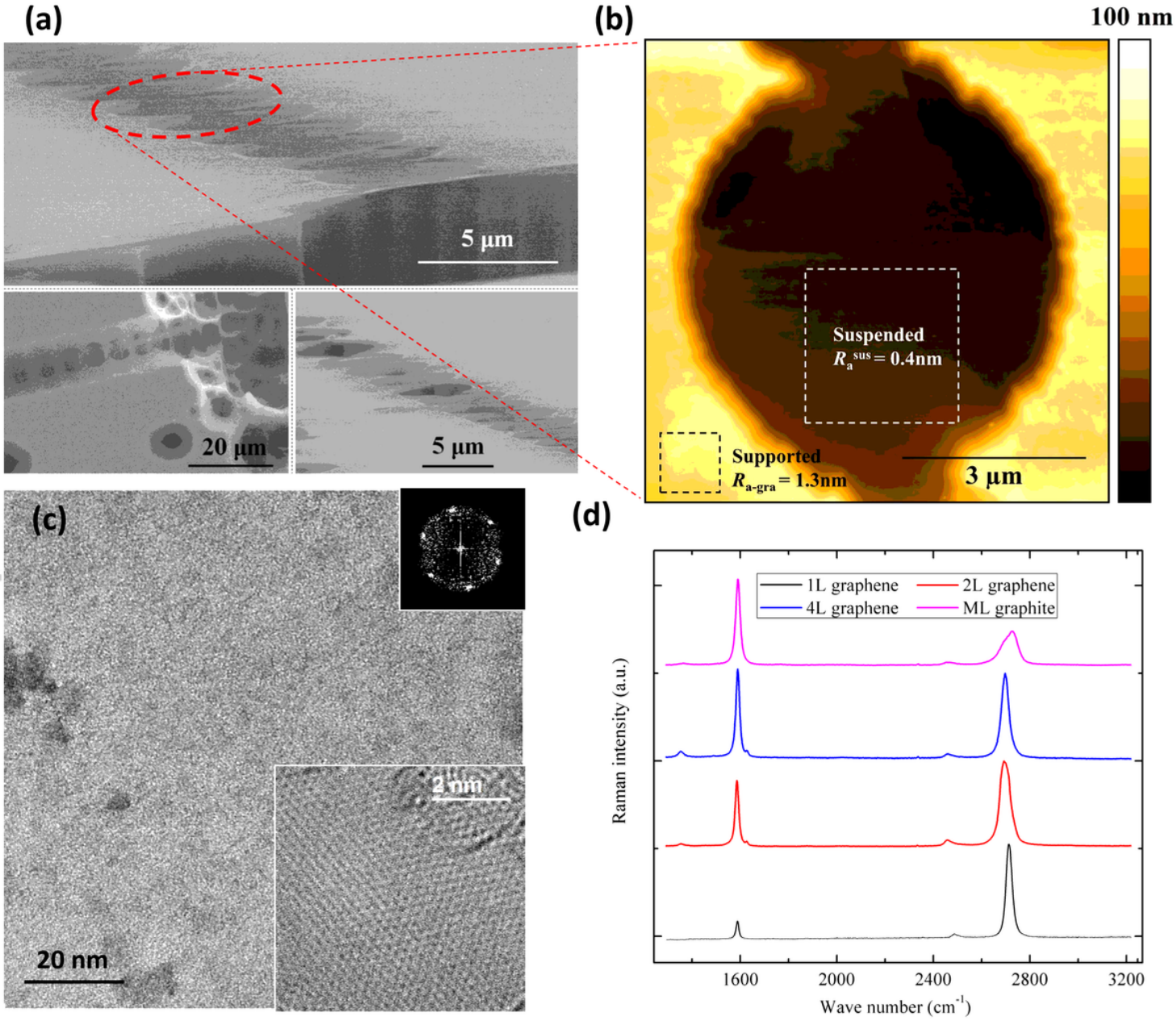

Figure 2

Surface characterization of 1L graphene by **(a)** SEM, **(b)** AFM height image of an area of 7.5×7.5 µm^2, **(c)** TEM and **(d)** Raman spectroscopy. Figure 2b also includes the root mean square surface roughness of suspended monolayer graphene, R_a^{sus} = 0.4 nm. Inset of Figure 2c bottom-right includes enlarged high-resolution TEM image and top-right shows electron diffraction (ED) pattern of 1L^{sus}. Figure 2d shows Raman spectra of 1L, 2L, 4L graphene and ML graphite, where the intensity ratio between 2D band

(~2700 cm^{-1}) and G band (~1580 cm^{-1}) correlates to number of layers with an I2D/IG ratio of nearly 5 for $1L^{sus}$ in agreement with Ref. 30.

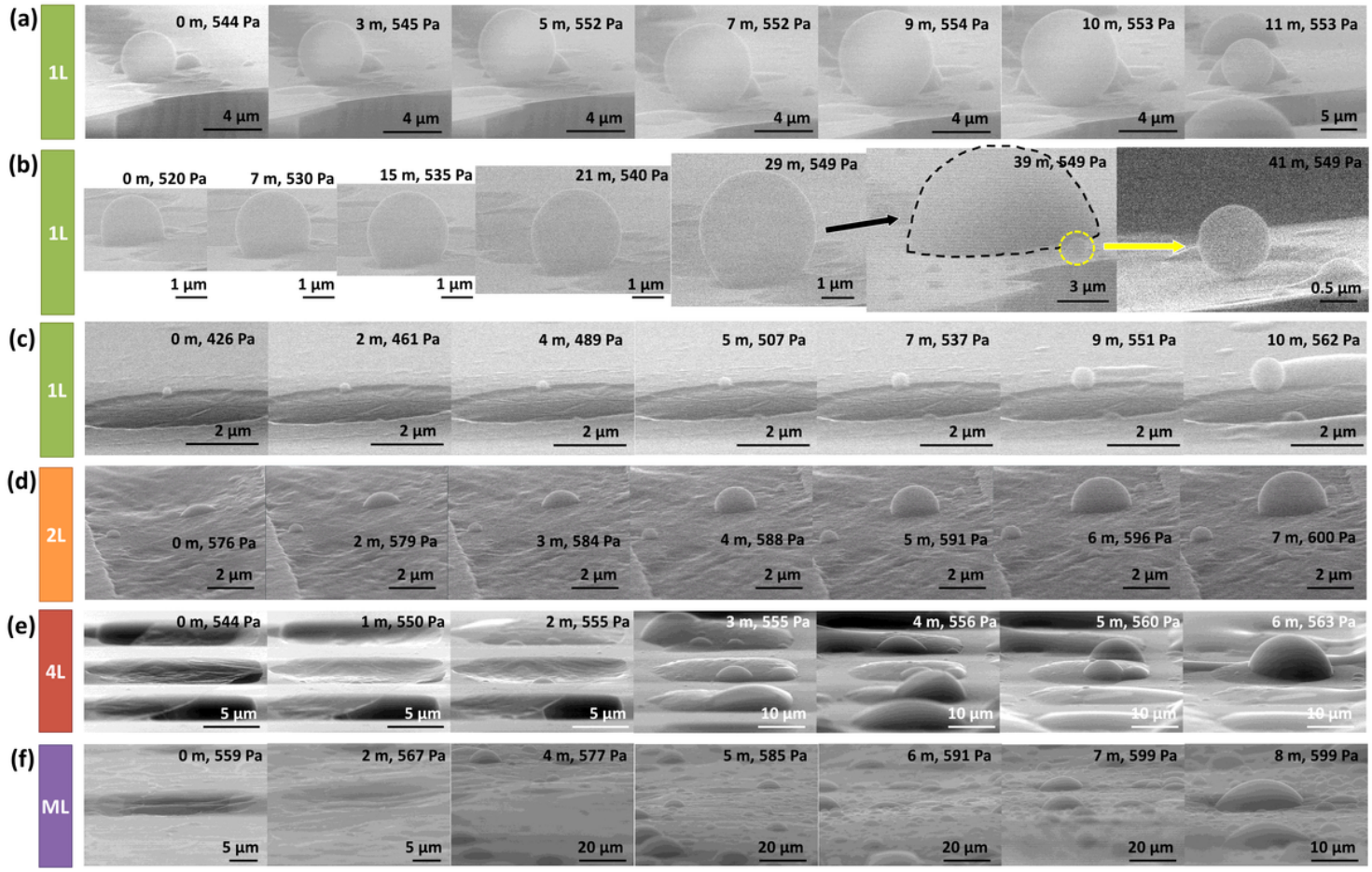

Figure 3

ESEM experimental observations of condensation on **(a-c)** $1L^{sus}$, (d) $2L^{sus}$, **(e)** $4L^{sus}$, and **(f)** ML^{sus} in time (see Supplementary Videos 1 to 6). Non-wetting water droplets are only observed on suspended graphene ($1L^{sus}$). We note here that experimental observations on **(a-b)** and **(c)** correspond to 2 different samples prepared by the same fabrication procedure reported in section 4.1 Sample Fabrication and in the accompanying Supplementary Information SI-1. Relative condensation time with respect to the first frame, environmental pressure and scale bars reported from ESEM experimental observations are included for each frame (more details on the ESEM experimental procedure and observations can be found in Section 4.3 ESEM Experimental Observations and within the Supplementary Information SI-3).

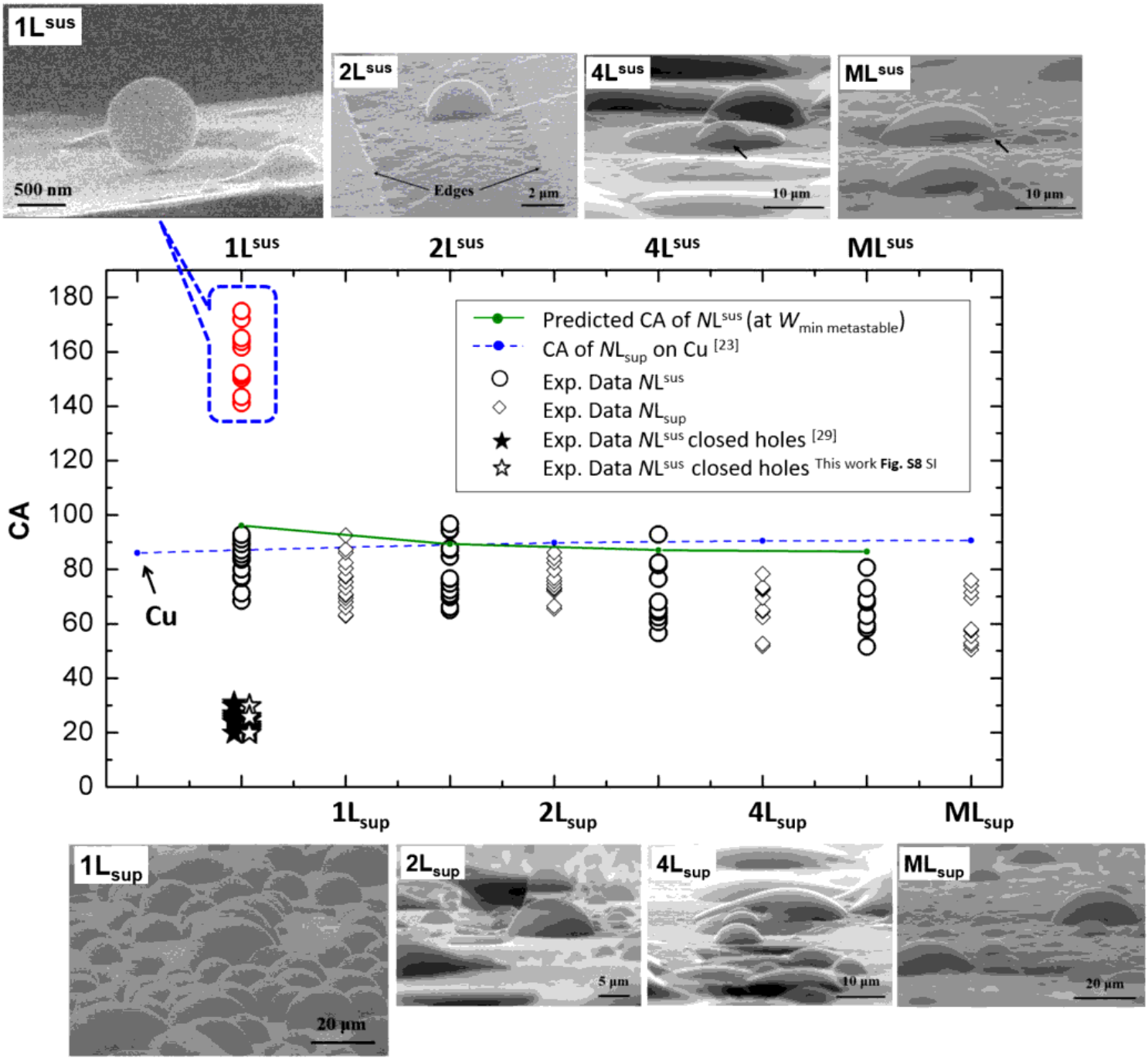

Figure 4

Wettability on supported and on suspended monolayer and multilayer graphene. (circles) Contact angles, CA or θ (deg), of droplets on suspended: $1L^{sus}$, $2L^{sus}$, $4L^{sus}$, and ML^{sus}, and (diamonds) contact angles of droplets on supported: $1L_{sup}$, $2L_{sup}$, $4L_{sup}$, and ML_{sup}. For each case, 10 to 20 independent CA measurements are reported. Theoretical CA trend based on the minimum Lennard-Jones (L-J) potential is plotted as a black solid line for comparison. While blue dashed line includes theoretical CA calculation of supported graphene on copper from Ref. 21. ESEM snapshots of (top) droplets on $1L^{sus}$, $2L^{sus}$, $4L^{sus}$ and ML^{sus} samples, and (bottom) droplets on $1L_{sup}$, $2L_{sup}$, $4L_{sup}$ and ML_{sup} samples are included for comparison. Non-wetting droplets on $1L^{sus}$ are represented as red circles. CA measurements of wetting

droplets on monolayer graphene suspended above a TEM grid with closed holes from (open stars) our work **Figure S8** and (closed stars) the work of Zhang et al. Ref. 29 are also included for comparison (note that the x-axis representation for suspended monolayer graphene with closed holes is slightly shifted so that the two conditions can be readily identified).

Supplementary Files

This is a list of supplementary files associated with this preprint. Click to download.

- VideoS6.avi
- 20220410SI.docx
- VideoS5.avi
- VideoS3.avi
- VideoS4.avi
- VideoS2.avi
- VideoS1.avi
- TOC.jpg